Three-dimensional effects in resonant charge transfer between atomic particles and nanosystems

I. K. Gainullin[1,*] and M. A. Sonkin[2]

[1]*Faculty of Physics, Moscow State University; Leninskie gory 1 # 2, Moscow 119992, Russia*

[2]*National Research Tomsk Polytechnic University, Lenin Avenue, 30, Tomsk 634050, Russia*

(Received 9 April 2015; revised manuscript received 29 June 2015; published 25 August 2015)

Resonant charge transfer (RCT) between negative ions and a metallic nanosystem was investigated by means of a high-performance *ab initio* three-dimensional (3D) numerical solver. During RCT, an electron was shown to occupy succesively nanosystem eigenstates along the z, ρ, and φ coordinates. Electron tunneling into a nanosystem is a reversible process, because after some time the electron propagates back to the ion. RCT efficiency in a nanosystem was found to exhibit quantum-size effects as well as lateral ion position dependence. This means that during ion-surface interaction, the nanosystem's size and the ion trajectory strongly influence the final charge state of the ion. In the case of real 3D systems (without cylindrical symmetry), the electron density currents form quantum vortices; this result is rather nontrivial for static systems. In addition, the limits of the adiabatic approximation (rate equation) for the RCT calculation with nanosystems are defined.

DOI: 10.1103/PhysRevA.92.022710 PACS number(s): 79.20.Rf, 34.35.+a, 73.40.Gk, 73.63.−b

I. INTRODUCTION

The investigation of electron transfer during the interaction between atomic particles and solid surfaces is of fundamental and practical importance in several branches of physics and chemistry. For fundamental science, electron transfer is of interest due to numerous phenomena such as scattering, sputtering, adsorption, and molecular dissociation [1–3]. The practical importance of electron transfer is stipulated by such applications as semiconductor miniaturization via thin-film deposition, reactive ion etching, catalysis, surface analysis tools (secondary ion emission), and modification [2,4–6]. In recent years, the electron transfer between atomic particles and surfaces containing adsorbates and nanosystems has been studied extensively. Surface nanosystems, e.g., metal-on-oxide, are important in many applications, such as heterogeneous catalysis, the fabrication of new ceramic materials, and solid-state gas sensors [7–9]. In the context of catalysis, one of the central questions involves the influence of a nanosystem's size and shape on its electronic structure and on the interaction with atoms and molecules [10].

Since the electron affinity level of atomic anions is significantly higher than the typical Fermi energy of most metallic surfaces, the transfer of an electron from an anion to the surface has a single-electron nature [11]. Thus, resonant charge transfer (RCT), i.e., energy-conserving one-electron tunneling through the potential barrier between an atomic particle and the surface, can be considered as a basic electron transfer mechanism for such systems [12]. The many-body aspects of RCT associated with the atomic structure of a projectile are usually taken into account by the inclusion of statistical factors [13,14]. The electron-electron interaction inside a metal can be accounted for by adding an artificial adsorbing complex potential [3].

The problem of RCT between an atomic particle and bulk metal has been explored intensively during the past two decades. The existing theory in most cases is in quantitative agreement with experimental data [3,6,11,15–24]. The calculations of RCT between an atomic particle and a solid body surface consider several aspects, including the following: (i) setting the initial charge state of the atomic particle, (ii) defining its trajectory, (iii) determining the pseudopotentials for the atomic particle, and (iv) the surface.

The influence of the initial charge state of the particle was studied in several experiments, and no memory effect of the initial charge state was found for typical atom/ion-surface combinations [15,16,26]. That is, regardless of the initial atomic particle charge state, only the RCT on the outgoing part of the trajectory is considered. In some studies, time-reversal symmetry is used to investigate the problem of electron loss by a neutral atom on the ongoing trajectory, instead of the problem of electron capture by a positive ion on the outgoing trajectory [19]. In many publications, the classical approach is used for atomic particle trajectory [17], in which a projectile moves along a straight line and the distance of closest approach is a parameter. However, there are also studies in which realistic trajectories are used, which take into account the ion interaction with image charge and where the distance of the closest approach depends on the projectile energy and the angle of incidence [6,11,25]. It should be noted that while the correct definition of the distance of closest approach is very important for the RCT calculation, the benefit from using a realistic trajectory is not evident (e.g., in Ref. [26], the benefit from using a realistic ionic trajectory does not exceed 10%).

The vast number of theoretical studies in this field consider the interaction of a one-active-electron atom or ion (e.g., H^0/H^-, Li^0/Li^+, Na^+, K^+), which can be modeled by analytical potential [27], with bulk metal. The analytical one-dimensional (1D) potentials have been constructed for two types of bulk metal surfaces: free-electron metals (the "jellium" model) [28] and metals with a projected band gap [29]. These potentials are called "1D" because they depend only on the distance to the surface. For the free-electron metals, tunneling along the surface normal is energetically favorable, and an atomic electron propagates indefinitely deep into the metal. In this case, there is no possibility for the reverse electron transition to the atom [30]. For a metal with a projected band gap, the electron motion along the surface normal is blocked [6,20], and the atomic electron decays via surface and image states [31,32]. In this case, the electron

*ivan.gainullin@physics.msu.ru

propagates mainly parallel to the surface, and RCT efficiency is less than that in the case of a free-electron metal. Note that 1D potentials cannot describe some experimental data, e.g., the azimuthal dependence of RCT probability [3,12]. In this case, it is necessary to use a realistic 3D potential, as was done in Refs. [33–35].

In the case of grazing scattering trajectories, the theory should take into account the frame transformation between the atomic particle and the surface [26], which can be illustrated by a shift of the Fermi spheres [36]. In this case, the electron translation factor is usually added into the wave function or rate equation [3,33]. The key result of these studies is the parallel velocity effect—RCT efficiency has a bell-shaped dependence on the velocity component parallel to the surface [3,12,26,37].

In many studies, the electron transfer probability is calculated by means of the rate equation, which can be applied under adiabatic conditions (adiabatic approximation) [12,15,17,19,38]. The core of the rate equation is that the electron transition rate at each moment is proportional to the atomic particle level width Γ. Under the adiabatic approximation, the atomic particle level width depends on the distance to the surface, but not on the projectile velocity. This is why the so-called "static problem" or fixed-ion approximation, when the atomic particle is fixed in front of the surface, has been widely investigated [11,17,19,39]. The main achievements for the static problem are the level width dependence on the ion-surface distance, the atomic level broadening [12,37,40–42], and the avoided crossing of the atomic particle electron's energy level with the discrete electron's energy levels inside the bulk metal [6,11,17,34,35].

The RCT between atomic particles and nanosystems is of interest, but this process has not been explored as thoroughly as RCT with bulk metals. In a metallic nanosystem, the electron energy is quantized and its motion is restricted as in the metals with a projected band gap [40,42,43]. Consequently, RCT efficiency is strongly affected by the nanosystem's energy level configuration, which depends on the nanosystem size. This leads to the quantum-size effect (or cluster-size effect), which consists of the nonmonotone dependence of the RCT efficiency on the nanosystem's size. In addition to the theoretical predictions [40,42,44–47], there are experimental observations of this effect [48,49]. In addition, there are some studies devoted to the RCT's lateral dependence [34,50].

An important issue in theoretical or numerical studies of RCT involves a numerical model and the dimension of the calculation domain. Most of the described studies were performed for 2D systems (3D with cylindrical or spherical symmetry). Three-dimensional RCT calculations were first mentioned in 2000 [51], but the reported system size (10^7 points) was too small to solve real 3D RCT problems. In addition, 3D calculations were reported in 2009, but their details and complexity are omitted [21]. The 3D RCT calculations with bulk metal using the Anderson-Newns model were reported in [34,35]. To the best of our knowledge, 3D calculations of RCT with nanosystems have not been explored in detail.

In this article, the RCT between an H^- ion and a thin Al island film in a fixed-ion approximation is investigated by means of an original high-performance *ab initio* 3D numerical solver [52]. Although the static problem is not realistic, it has a large fundamental impact because this model problem allows us to investigate the basic RCT features. The thin disk has been chosen as a geometrical model of the island film. In Ref. [53], it was shown that under electron irradiation, Al island films are formed on the Al_2O_3 surface. The island's geometrical form is close to circular; moreover, the average circle size depends on the irradiation dose. The described system and its model have been investigated previously by means of 2D calculations methods [38–40,43,45]. Therefore, in addition to the results of 3D calculations, we will discuss their differences with previous 2D calculations for the cylindrically symmetrical problem (the H^- ion is located on the island film symmetry axis). Section II describes the problem and the numerical method. Section III contains the eigenproblem analysis for the island film. Section IV is devoted to the RCT resulting from the 3D calculations for the cylindrically symmetrical problem, and Sec. V addresses the results obtained for the asymmetrical problem. In Sec. VI, the results of a dynamical study are given. Finally, Sec. VII contains concluding remarks. For convenience, the atomic system of units (with $m_e = e = \hbar = 1$; 1 a.u. of distance is equal to 0.53 Å, 1 a.u. of time is equal to 2.419×10^{-17} s, and 1 a.u. of velocity is equal to 2.188×10^8 cm/s) is used in this article.

II. THE PROBLEM FORMULATION AND THE NUMERICAL METHOD

A. The problem formulation

The problem of the study is shown in Fig. 1. The H^- ion is fixed in front of a thin island film at the distance Z to the film surface and at the distance X to the film symmetry axis. A disk of thickness D and radius R is selected as a geometrical model of the island film. The problem is solved in Cartesian coordinates x, y, and z, but the cylindrical coordinates z, ρ, and φ are also shown in order to interpret the RCT results. For most examples in this study, the film thickness was set to 15 a.u., the film radius was set to 50 a.u., and the distance to the film was set to 12 a.u. The choice of parameters is stipulated by the values used in previous studies.

At the initial moment, the electron is located on the affinity level of the H^- ion, and RCT begins due to the influence of the H^- and Al film potentials. The H^- potential $V_{H^-}(r) = -(1 + 1/r)\exp(-2r) - (\alpha_H/r^4)\exp(-r_0^2/r^2)$ is the interaction potential between an electron and an atomic core (r is the radial electron-atom distance in atomic units, $\alpha_H = 2.25$, and $r_0^2 = 2.547$) [54,55]. The interaction potential between an electron and a thin Al island film $V_{e\text{-surf}}$ is calculated as the conjunction of the conduction-band bottom ($U_0 = 15.9$ eV) with a classical self-image potential of the electron $-1/4\,z$ (the so-called "Jennings" potential):

$$V_J(z) = \begin{cases} \frac{1-\exp(\lambda z)}{4z} & \text{if } z < 0, \\ \frac{-U_0}{1+A\exp(-Bz)} & \text{if } z \geqslant 0, \end{cases} \tag{1}$$

where $B = U_0/A$, $A = -1 + 2U_0/\lambda$, and the parameters U_0 and λ are defined for certain metals, including Al [28]. To construct the potential of a thin film with two borders, the following conversion is used: $V_{e\text{-film}}(z) = V_J(|z - T/2|)$. Finally, the superposition of Jennings potentials along normal and polar coordinates is used in order to obtain the two-dimensional potential $V_{e\text{-surf}}(z, \rho)$. When the island film

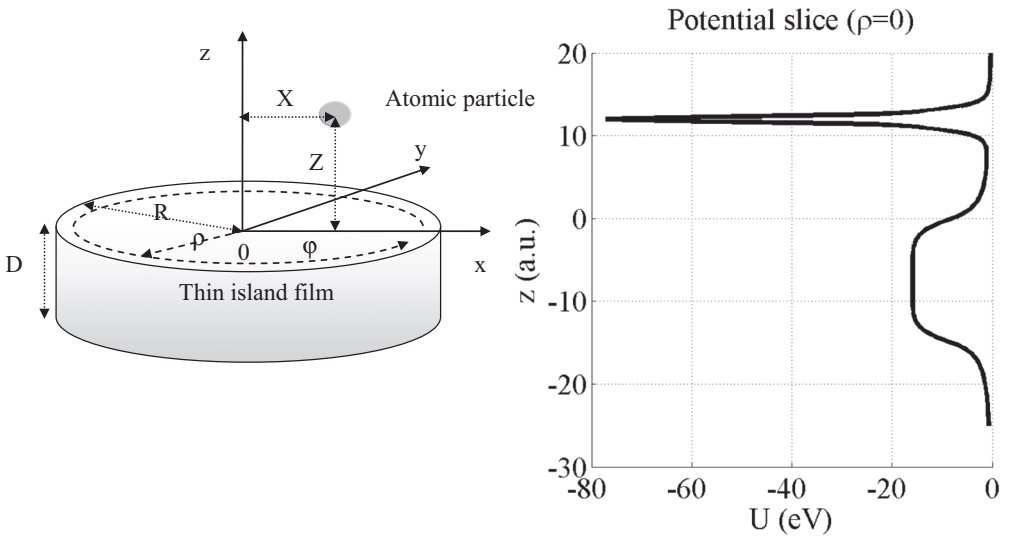

FIG. 1. Illustration of the problem. Left: in the Cartesian coordinates, the atomic particle is fixed in front of the thin island film. D is the film's thickness, R is the film's radius, Z is the distance between the atomic particle and the nearest film's surface, and X is the distance between the atomic particle and the island film's symmetry axis. Dashed arrows labeled ρ and φ correspond to the cylindrical coordinates. Right: example of potential slice ($X = 0$, $y = 0$) for the system with $D = 15$ a.u., $Z = 12$ a.u., and $X = 0$.

radius is extremely large, the potential becomes identical to the potential of a film of the same thickness. The slice of total system potential is shown in the lower part of Fig. 1.

B. Numerical method

The RCT calculation is based on the numerical solution of the time-dependent Schrödinger equation (TDSE). In this research, we use an original high-performance *ab initio* 3D numerical TDSE solver, which utilizes graphical processing units. Details on the TDSE solver's parallel implementation, verification, performance, and scalability are given in Ref. [52]. Here we describe only the numerical scheme.

To solve the TDSE in Cartesian coordinates, we use the explicit propagation scheme, which is also known as the "leapfrog" scheme. It is the second-order differencing (SOD) scheme [56].

Consider the TDSE in the form

$$i\frac{d\psi(\vec{r},t)}{dt} = H(t)\psi(\vec{r},t), \tag{2}$$

with the Hamiltonian

$$H = -\frac{\nabla^2}{2} - U(\vec{r},t), \tag{3}$$

where $U(\vec{r},t) = V_{\mathrm{H}^-}(\vec{r}) + V_{e\text{-surf}}(\vec{r})$ is the time-dependent potential.

The time-evolution scheme appears as

$$\phi^{n+1} = -2i\tau[H\phi^n] + \phi^{n-1}, \tag{4}$$

with initial conditions

$$\begin{aligned}\phi^0 &= \psi_0 + \frac{i}{2}\left[H\left(\frac{\tau}{2}\right)\psi_0\right],\\ \phi^1 &= \psi_0 - \frac{i}{2}\left[H\left(\frac{\tau}{2}\right)\psi_0\right],\end{aligned} \tag{5}$$

where ϕ is a spatial discretization of the electron wave function, ψ_0 is an initial state (normalized ground-state wave function), and τ is a time step.

To prevent the time oscillations of the wave function due to reflections from the borders, the absorbing image potential $V(\vec{r})$ is used, which modifies the time-evolution scheme in the following way:

$$\phi^{n+1} = -2i\tau e^{-i\tau V}[H\phi^n] + e^{-2i\tau V}\phi^{n-1}. \tag{6}$$

Because "leapfrog" is only an SOD scheme, the important question is its accuracy. The verification shows that the integration error after 10^6 time steps does not exceed 1% (precision of about 10^{-8} per time step), which is satisfactory for the problems under study.

C. Extraction of the RCT characteristics and analysis of the calculation results

The main characteristics of the RCT are the energy level (E) and level width (Γ). The level width characterizes the probability of electron transfer per unit of time ($\Gamma \sim 1/\tau$, where τ is the lifetime of the initial state). A very simplified qualitative interpretation of the RCT process is that the initial electron state decays by the exponential law

$$\psi(r,t) = \psi_0(r)\ \exp(-i\,Et)\ \exp(-\Gamma t). \tag{7}$$

The numerical scheme of the TDSE solver provides the time evolution of the system's wave function $\psi(\vec{r},t)$. If we project the current wave function on the initial state of the system $\psi_0(r)$, we will obtain an autocorrelation function,

$$A(t) = \langle\psi_0(r)\,|\,\psi(r,t)\rangle, \tag{8}$$

which is a complex function. Its real and imaginary parts oscillate in time with a frequency equal to the energy level of an electron, and its modulus is the probability that a system remains in the initial state. This means that $|A(t)| = 1$

corresponds to a situation in which the electron occupies the hydrogen affinity level, while $|A(t)| = 0$ means that the outer H^- electron has completely gone into the nanosystem.

The more sophisticated interpretation of the RCT process deals with the Fourier transform of the autocorrelation function,

$$g(\omega) = \frac{1}{\pi}\int_0^\infty dt\, e^{i\omega t} A(t) = \frac{1}{\pi}\int_0^\infty dt\, e^{i\omega t}\langle\psi_0(r)\,|\,\psi\,(r,t)\rangle, \tag{9}$$

which is the complex function of the oscillation frequency (electron energy). The modulus of $g(\omega)$ gives the distribution of the energy-level occupation. In the case of nanosystems, the ion occupation probability $|A(t)|$ oscillates in time, even for large propagation times $|A(t)| > 0$. This means that the Fourier transform of the autocorrelation function will contain side lobes in addition to the main peak. To suppress the side lobes, we use the Hamming window,

$$\begin{aligned} g(\omega) &= \frac{1}{\pi}\int_0^\infty dt\, e^{i\omega t} A(t) f(\omega), \\ f(\omega) &= 0.54 - 0.46\ \cos(2\pi/T_{\max}), \end{aligned} \tag{10}$$

where $T_{\max}$ is the propagation time. To extract the level width, we calculate the incline of $\ln|A(t)|$ on the linearly descending section. The numerical experiments with the test data give an error estimation of the described procedure of about 2%.

D. Eigenenergies and eigen wave function calculation

Additional important points for the interpretation of the RCT calculation results are the eigenenergy levels E_k and eigen wave functions $\Psi_k(\vec{r})$ of the electron inside the nanosystem. To calculate the eigenenergy levels, we need to solve the time-independent Schrödinger equation (TISE),

$$H\psi(\vec{r}) = E_k\psi(\vec{r}). \tag{11}$$

The finite-difference form of the TISE in the Cartesian coordinates is as follows:

$$-\frac{\psi_{l+1,m,n} + \psi_{l-1,m,n} + \psi_{l,m+1,n} + \psi_{l,m-1,n} + \psi_{l,m,n+1} + \psi_{l,m,n-1} - 6\psi_{l,m,n}}{2h^2} + U_{l,m,n}\psi_{l,m,n} = E_k\psi_{l,m,n}, \tag{12}$$

where h is the discretization step along the spatial coordinates.

To solve the TISE numerically, we transform the 3D array $\psi_{l,m,n}$ to a 1D vector f_i, where $i = (l-1)\times(N\times M) + (n-1)\times(M+m)$, and L, N, and M are the dimensions of the $\psi_{l,m,n}$ array. Therefore, the TISE transforms to the matrix equation

$$[A]\times\{f\} = E_k\{f\}, \tag{13}$$

where A is a square seven-diagonal sparse matrix of size $(L\times N\times M)\times(L\times N\times M)$.

The eigenvalues and eigenvectors of matrix A give the eigenenergies and eigen wave functions of the TISE. The choice of the Dirichlet boundary condition, $\psi_{0,m,n} = \psi_{L+1,m,n} = \psi_{l,0,n} = \psi_{l,M+1,n} = \psi_{l,m,0} = \psi_{l,m,N+1} = 0$, or the von Neumann boundary condition, $\psi_{0,m,n} = \psi_{1,m,n}$; $\psi_{L+1,m,n} = \psi_{L,m,n}$; $\psi_{l,0,n} = \psi_{l,1,n}$; $\psi_{l,M+1,n} = \psi_{l,M,n}$; $\psi_{l,m,0} = \psi_{l,m,1}$; $\psi_{l,m,N+1} = \psi_{l,m,N}$, does not affect the results significantly.

Note that for the 3D eigenproblem for the nanosystems under study (with a linear size of about 100 a.u.), the characteristic size of matrix A is $10^8\times10^8$, and its numerical solution is rather resource-consuming. Because the system under study (a thin island film) has cylindrical symmetry, the TISE transformation to the cylindrical coordinates ρ, z, and φ reduces the complexity of the problem,

$$-\frac{1}{2}\left(\frac{\partial^2\psi}{\partial\rho^2} + \frac{1}{\rho}\frac{\partial\psi}{\partial\rho} + \frac{\partial^2\psi}{\partial z^2} + \frac{1}{\rho^2}\frac{\partial^2\psi}{\partial\varphi^2}\right) + U(\vec{r})\cdot\psi(\vec{r}) = E_k\psi(\vec{r}). \tag{14}$$

Here we use the periodic boundary conditions for the φ coordinate $\psi_{0,m,n} = \psi_{L,m,n}$. The boundary conditions for $\rho\to0$ are defined as $(\partial^2\psi/\partial\rho^2)(\rho\to0) = 0$, or $\psi_{l,m,0} - \psi_{l,m,1} = \psi_{l,m,1} - \psi_{l,m,2}$. It should be noted that if we set $\rho_1 = 0.5h$, the above boundary conditions are equal to the simple "natural" condition $\psi_{l,m,0} = \psi_{l',m,1}$, where l',m, 1 is the point symmetrical to l,m, 1.

Numerical experiments have shown that the spatial discretization step $h = 0.2$ a.u., and the halo size 10 a.u. (distance from the border of the film to the border of the calculation domain) gives the eigenenergies of the thin island film with a precision of about 0.1%. More details on the eigenenergy calculations can be found in Ref. [57].

E. Visualization aspects for 3D electron distribution

For the visualization of the electron density spatial distribution, we use isosurfaces of electron density for some chosen value. This is the most suitable (albeit not perfect) form of visualization of the 3D function in journal format ("static 2D"). The large as well as small values chosen for the isosurface can hide some major aspects of the electron density distribution.

To visualize the electron current density, we use the 2D field vector plot in the x-y coordinates, where electron current is averaged along the z coordinate.

For the electron current calculation, we use the following formula:

$$\vec{j}(r,t) = \frac{1}{2i}\cdot[\psi^*(\vec{r},t)\cdot\vec{\nabla}\psi(\vec{r},t) - \psi(\vec{r},t)\cdot\vec{\nabla}\psi^*(\vec{r},t)]. \tag{15}$$

For the calculations of the electron current component along certain coordinates, we use the corresponding scalar product averaged in the calculation domain. Note that for the φ current component, the modulus of the scalar product was averaged, so this component can be treated as rotational energy around the symmetry axis of the island film.

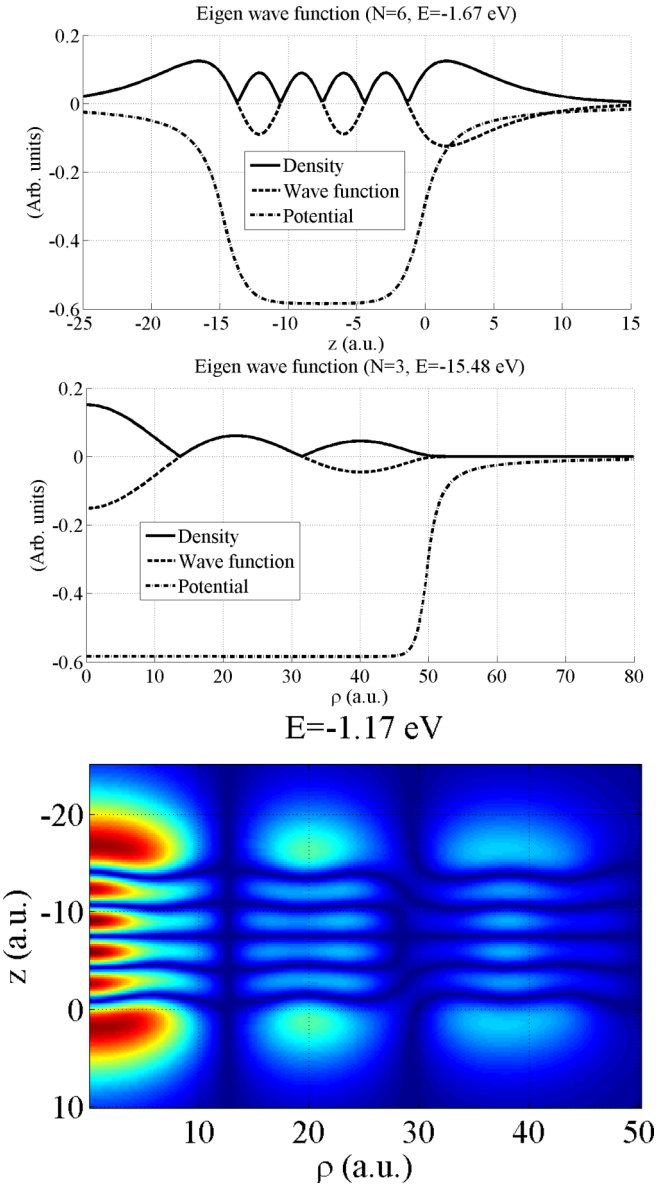

FIG. 2. (Color online) 1D and 2D eigen wave functions for the thin Al film of thickness 15 a.u. and radius 50 a.u. Upper and middle: eigen wave functions and electron densities along z and ρ coordinates obtained for the 1D eigenproblem. Lower: eigen wave function along z and ρ coordinates obtained for the 2D eigenproblem.

III. EIGENENERGIES AND EIGEN WAVE FUNCTIONS OF THE THIN ISLAND FILM

The numerical results in this section are obtained for the Al island film of 15 a.u. thickness and 50 a.u. radius.

A. One- and two-dimensional case

Analysis of the 1D (z coordinate) and 2D (ρ-z coordinates) eigenstates helps us to understand the specificity of the eigenstates in the 3D case. 1D and 2D eigenstates are obtained as the TISE solution in the 1D and 2D case, respectively.

Figure 2 contains the electron density of the selected eigenstate for the z, ρ, and ρ-z coordinates. The choice of eigenstates corresponds to the results described in the following sections. The eigen wave functions and potential are also shown for the 1D problem. We see that for the 1D problem, the solution has a harmonic character and is similar to the classic problem of quantum mechanics. The 1D eigenstates for the z coordinate correspond to the eigenstates inside an infinite thin film. The interesting feature is that a significant part of the electron density is located outside the film ($-15 < z < 0$ a.u.). Such localization is typical for all of the eigenstates, not only for the selected one. The spatial localization of the eigenstates outside the nanosystem can be treated as an analog of the images states in the case of metals with a projected band gap. Notably, such localization occurs only for z, but not for the ρ coordinate.

Also, Fig. 2 shows that for the considered potential of the Al island film, the 2D eigen wave function can be expressed as multiplication of two 1D eigen wave functions ("z, ρ eigen wave function") along each coordinate, and the 2D eigenenergy level is a sum of two 1D eigenenergies:

$$\Psi_n(\vec{r}) \approx \Psi_i(z)\Psi_j(\rho), \quad E_n \approx E_i^z + E_j^\rho. \tag{16}$$

To fulfill the above equation, the energy levels relative to the vacuum ($E = 0$ eV) should be converted to the energy levels relative to the bottom of the Al film potential ($E = -15.9$ eV).

B. Three-dimensional case

Figure 3 contains the examples of 3D eigenstates. We see that harmonics along the φ coordinate appear. However, for practical usage, the 2D ρ-z slices are more suitable. Figure 4 contains such slices for the eigenstates corresponding to the TDSE results in the following sections. All of them have six maxima of electron density along the z coordinate (this is stipulated by the sequence of eigenstate occupation in the dynamic case). We see that there are two groups of eigenstates:

(i) "Central" states ($E = -1.17$, -1.43, and -1.61 eV)—when the electron density is located near the symmetry axis and does not depend on the φ coordinate. It should be noted that these states are equal to the 2D eigenstates obtained for the z-ρ coordinates.

(ii) "Peripheral" states ($E = -1.16$, -1.19, -1.21, -1.29, -1.32, and -1.37 eV)—when the electron density near the symmetry axis is close to zero, and the eigen wave functions depend on the φ coordinate.

The spatial localization of the electron density for the "peripheral" states is a bit unexpected, because $\Psi_n(\vec{r}) \neq \Psi_i(z)\Psi_j(\rho)\Psi_k(\varphi)$ as one can expect by parity of reasoning with the 1D and 2D cases. The possible explanation for such a dependence is that a member of TISE $(1/\rho^2)(\partial^2\psi/\partial\varphi^2)$ seeks infinity for $\rho \to 0$ unless $\partial\psi/\partial\varphi \neq 0$. Hence, two types of eigenstates can be realized: if $\psi(\rho \to 0) \neq 0$, then $(\partial\psi/\partial\varphi)(\rho \to 0) = 0$ and the TISE solution gives "central" states, which do not depend on φ; otherwise, the TISE solution gives "peripheral" states.

In conclusion, for the precise analysis of TDSE results, we should use the TISE eigenstate obtained for the same potential, i.e., not the isolated island film but rather the island film and the neighbor ion (see Fig. 1). The comparison shows that the TISE results for the described complex system are very similar to the TISE results for the lone island film (the difference in the eigenenergies is less than 0.02 eV).

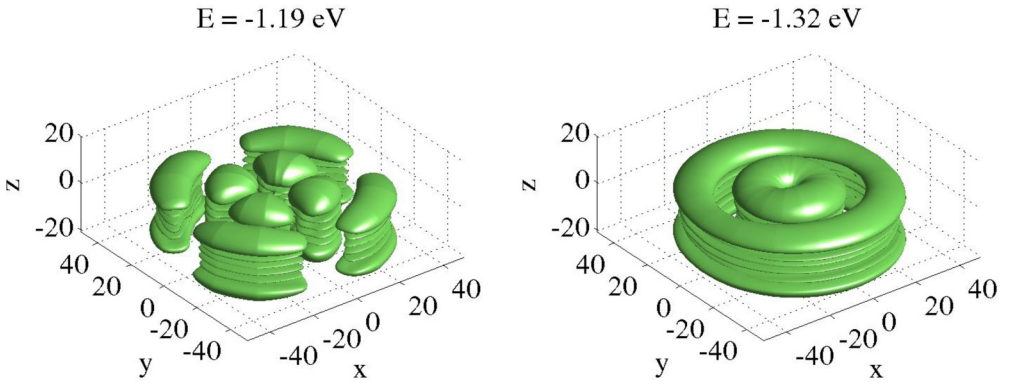

FIG. 3. (Color online) 3D eigen wave functions (electron density) for the thin Al film of thickness 15 a.u. and radius 50 a.u. Isosurfaces for the electron density equal to half of the maximal density are shown; the values of the axes x, y, z are given in atomic units.

IV. RESONANT CHARGE TRANSFER FOR THE CYLINDRICALLY SYMMETRIC PROBLEM

This section contains the results of 3D RCT calculations for the cylindrically symmetric problem. Some examples are compared to the results of the 2D calculations for the same systems. The 2D calculations were performed previously by the corresponding author by means of the wave-packet-propagation method and reported in Refs. [43,45].

A. Evolution of the electron density and ion state survival probability

Figure 5 represents the evolution of the electron density spatial distribution in the symmetrical case. This evolution can be divided into four stages: (i) During the first stage (0−50 a.u.), the electron propagates into the nanosystem along the z direction without any restrictions, and the electron density distribution is continuous. (ii) During the second stage (50−150 a.u.), the electron reaches the remote nanosystem

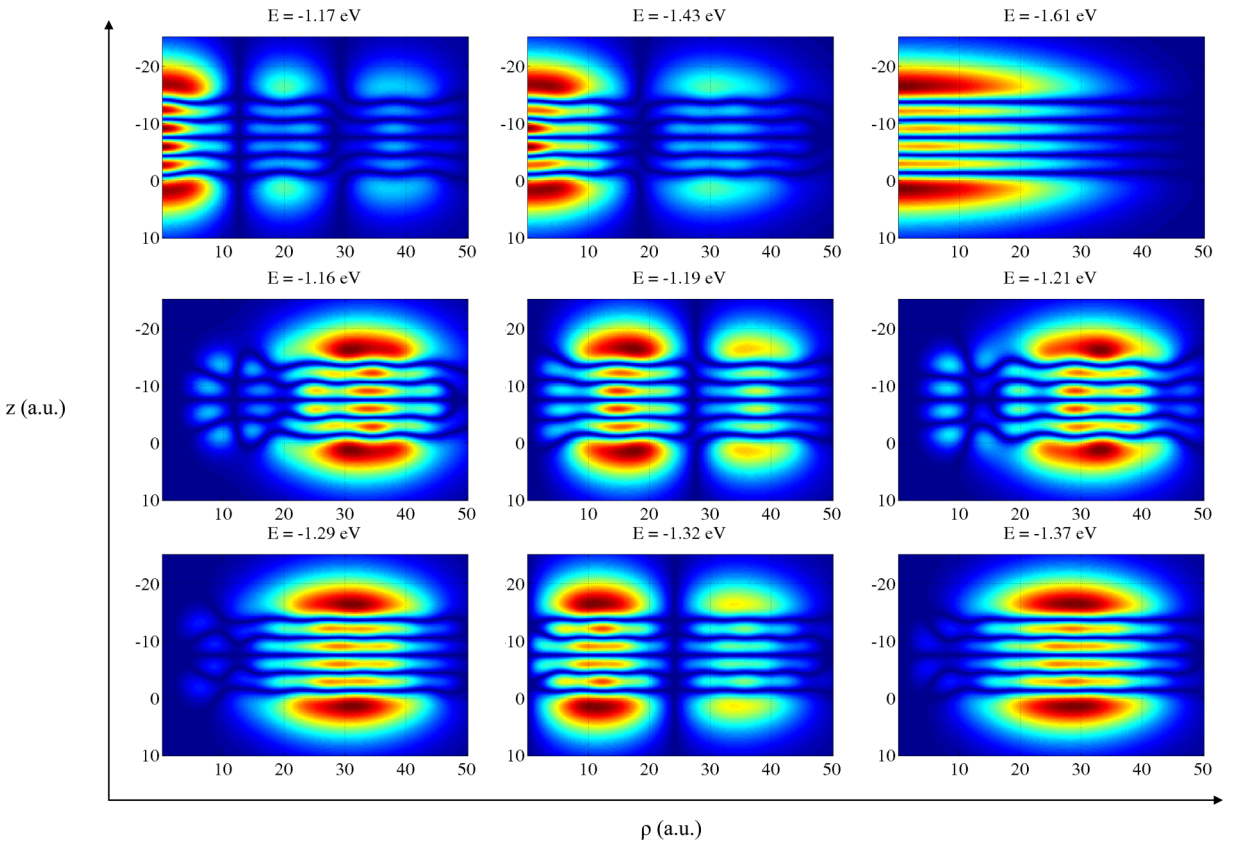

FIG. 4. (Color online) 2D projection of 3D eigen wave functions (electron density) for a thin Al film of thickness 15 a.u. and radius 50 a.u. Each slice shows an electron density projection on the z-ρ plane (choice of φ value corresponds to the maximum of the 3D electron density).

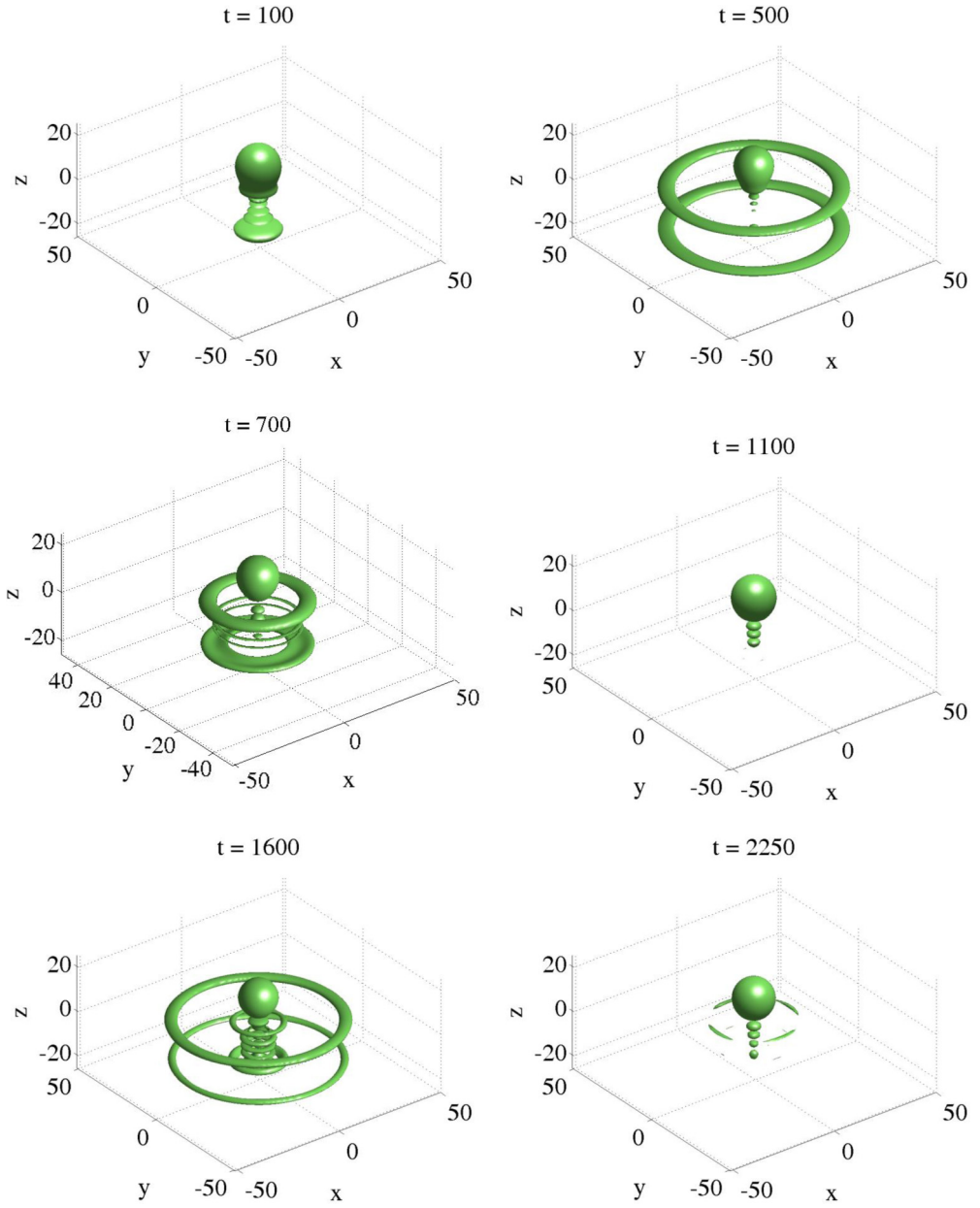

FIG. 5. (Color online) Isosurfaces of the electron density ($\rho = 0.0001$) at the subsequent moments of time for the cylindrical symmetry case ($X = 0$). The ion coordinates are (0,0,12) a.u., and the island film borders are $z = 0$ a.u., $z = -15$ a.u., and $x^2 + y^2 = (50\,\text{a.u.})^2$. The values of the axes x, y, z and t moments are given in atomic units.

border and starts to propagate mainly along the ρ direction, and 1D maxima appear along the z coordinate. (iii) During the third stage (150−2000 a.u.), the electron reaches the radial borders of the nanosystem, and 2D maxima appear along the z-ρ coordinates. (iv) During the fourth stage (more than 2000 a.u.), the electron density exhibits 3D maxima along the z-ρ-φ coordinates. Due to the aspects of electron density visualization, the electron density as shown in Fig. 5 has a different number of maxima along the z coordinate for different times. However, the precise calculation of the averaged electron density shows that during stages 2–4, it has six maxima along the z coordinate. This means that the electron preserves the z-harmonic received at stage 2. In addition, it should be stressed that the electron density distribution exhibits two maxima outside the film borders, which is analogous to the image states for the metals with the projected band gap.

The matching of the spatial distribution of the electron density (mainly by maxima along the ρ coordinate) shows that the electron density is relevant to different eigenstates for different time moments. More precisely, the electron density distribution inside the nanosystem is a superposition of densities of several relevant eigenstates and a moving part of the wave packet. Initially the electron populates the "1D" eigenstate $E = -1.61$ eV (stage 2). This is not surprising, because RCT between an ion and a nano-object in the symmetrical case is likely to occur via "central" states.

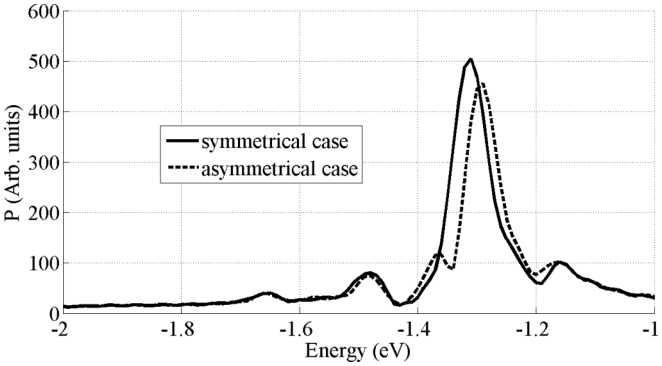

FIG. 6. Energy spectrum for the symmetrical ($X = 0$) and asymmetrical ($X = 5$ a.u.) cases. The ion coordinates are (0,0,12) and (5,0,12) a.u. respectively; the island film borders are $z = 0$ a.u., $z = -15$ a.u., and $x^2 + y^2 = (50\,\text{a.u.})^2$.

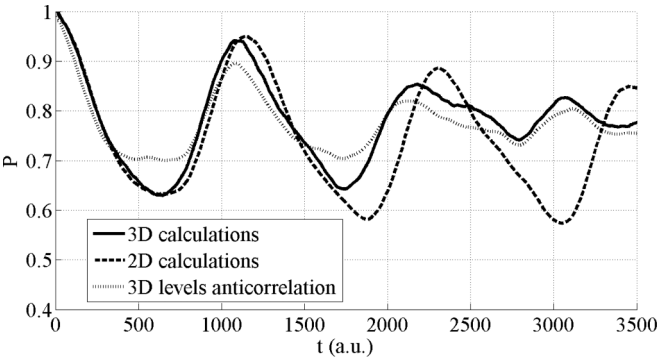

FIG. 7. Probability of the H^- state survival as a function of time for the cylindrical symmetry case ($X = 0$). The solid line represents the results of 3D calculations; the dashed line represents the results of 2D calculations (in polar coordinates z-ρ); the dotted line represents electron density anticorrelation with 3D eigen wave functions in arbitrary units.

In stage 3, the "2D" electron density maxima appear. Note that the depicted electron density maxima (rings) do not reflect the motion of the wave packet, but they remain stable for several hundreds of atomic units of time. For example, for $t = 500$ a.u. (rings near $\rho = 33$ a.u.), the eigenstate with $E = -1.21$ eV dominates; for $t = 700$ (rings near $\rho = 17$ a.u.), the dominated eigenstate is $E = -1.19$ eV. At the moment $t = 1600$ a.u. (rings near $\rho = 31$ and 11 a.u.), two eigenstates with energies $E = -1.32$ and -1.29 eV are visible. The above energies of eigenstates are confirmed by the energy spectrum of the autocorrelation function (Fig. 6). It has maxima near -1.31, -1.16, -1.48, and -1.65 eV. The main peak corresponds to the energy level of the hydrogen anion located at 12 a.u. from a metallic surface ($-1.32\,\text{eV} = 0.75\,\text{eV} + 27.211\,\text{eV}/4 \times 12\,\text{a.u.}$). The other peaks correspond to different eigenstates shown in Fig. 4.

Note that the sequence of eigenstate occupation ($E = -1.21$, -1.19, and -1.32 eV) does not correspond to the energy proximity to the ionic level (-1.32 eV). The radial eigenstate occupation occurs as a result of wave-packet reflection from the film's boundary, which is why the eigenstate with the largest radius of electron density became populated first.

Note that during the third stage, the electron density distribution does not depend on the φ coordinate, but for the moments when the electron is distributed across the film, the spatial localization of the electron density is close to the φ-dependent "peripheral" states ($E = -1.21$, -1.19, -1.32, and -1.29 eV) rather than to the φ-independent "central" states. More surprising is that for the 2D calculations (z-ρ coordinates), the electron density maxima along the ρ coordinate also correspond to the 3D "peripheral" states. To solve this paradox, let us look at the TISE equation in the cylindrical coordinates:

$$-\frac{1}{2}\left(\frac{\partial^2\psi}{\partial\rho^2} + \frac{1}{\rho}\frac{\partial\psi}{\partial\rho} + \frac{\partial^2\psi}{\partial z^2} + \frac{1}{\rho^2}\frac{\partial^2\psi}{\partial\varphi^2}\right) + U(\vec{r})\psi(\vec{r}) = E_k\psi(\vec{r}).$$

For large ρ ($\rho > 10$ a.u.), the member $(1/\rho^2)(\partial^2\psi/\partial\varphi^2)$ is significantly less that other derivatives. Hence the approximate TISE solution can be obtained, $\psi(z,\rho) \approx \int d\varphi\ \psi(z,\rho,\varphi)$, which does not depend on the φ coordinate. This solution does not satisfy the precise TISE equation, but it has a physical meaning for the dynamic situation (TDSE) in which the electron density near $\rho = 0$ changes in time rapidly due to the interaction with the ion. Thus, in the dynamic situation, the pseudo-3D states arise, which have localization close to the real 3D states, but they do not depend on the φ coordinate. From a mathematical point of view, the pseudo-3D states can be obtained by solving the TISE on a ring [e.g., $\partial\psi/\partial\rho(\rho = 10\ \text{a.u.}) = 0$].

It should be noted that even under 2D initial conditions and potential (cylindrically symmetric), the system evolves to the 3D state with electron density maxima along all three coordinates. This is a fundamental difference with the 2D calculations. Of course, the electron density distribution preserves cylindrical symmetry for a long time (up to 2000 a.u.), so for the realistic interaction times the RCT in the symmetrical case can be described by 2D calculations, where the electron interacts with 2D continua of the nanosystem. The calculations of the electron current along the z, ρ, and φ coordinates do not show any interesting dependences. The only fact that should be mentioned is that the electron current along the φ coordinate is three orders of magnitude less that the electron current along the z and ρ coordinates. After $t = 1500$ a.u., j_φ increases approximately twofold. Another interesting feature of RCT in the symmetrical case is its "reversibility". Figure 7 shows the survival probability of the H^- state (or ion occupation) as a function of interaction time [modulus of autocorrelation function; see Eq. (8)]. We can see that in the first stage of interaction, the electron decays from an atomic particle into the nanosystem, but in the second stage the reverse process begins—the electron moves back to the atomic particle. Note that this process has an oscillatory characteristic, i.e., the ion occupation is a periodic function of time. The oscillation period (~1100 a.u. for the system under study) is equal to the electron reflection time, i.e., the time necessary for the wave packet of the electron to propagate to the remote nano-object boundary and to return. The oscillation amplitude, which defines the minimal ion survival probability, depends on the RCT efficiency. It is approximately equal to the portion of the

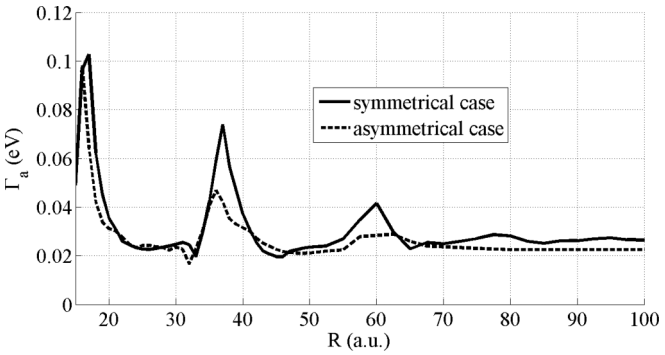

FIG. 8. H^- level width as a function of island film radius for the symmetrical ($X = 0$) and asymmetrical ($X = 5$ a.u.) cases.

electron density tunneled to the nanosystem during half of the electron reflection time. One can see that the ion occupation exhibits anticorrelation with the occupation of "peripheral" states. This fact indicates that for the symmetrical problem ($X = 0$), RCT between the ion and the nanosystem occurs via "central" states. In other words, when the electron is located on the "peripheral" state, it cannot transfer back to the ion.

Also in Fig. 7, the results of 2D calculations are shown. We see that oscillations in the 2D case have a slightly different period and are more regular (oscillation amplitude remains the same). The maximal ion-survival probability decreases monotonically because the electron reflection in the nanosystem is not perfect, and during each cycle, the definite portion of the electron density remains in the nanosystem. The attenuation of the oscillation amplitude after 2000 a.u. of time in the 3D case is explained by the more stable occupation of the "peripheral" eigenstates, which is accompanied by the increase of the j_φ current component.

B. Quantum-size effect observation and interpretation

Figure 8 demonstrates the H^- level width (RCT efficiency) as a function of the island film radius. We see that this dependence is nonmonotone and the RCT efficiency can vary up to four times with the nanosystem size. This dependence is called the quantum-size effect, and it is similar to the 2D case dependence, reported in Ref. [45]. The small subpeak near the maxima at $R = 32$ a.u. is interpreted as an artifact of the H^- level width extraction procedure, and it does not have a physical meaning.

The qualitative explanation of the quantum-size effect is based on the discrete energy structure of the nanosystem. During RCT, the H^- electron successively occupies the nanosystem's eigenstates along the z, ρ, and φ coordinates. For the film of 15 a.u. thickness, initially the energy state with energy -1.61 eV (see Fig. 4) is occupied, which corresponds to the electron transition into the infinite thin film. Because of the energy conservation law, the electron wave packet acquires some kinetic energy (the difference between ionic levels -1.32 and -1.61 eV) preferably in the direction parallel to the surface. When the higher harmonic of the electron's de Broglie wavelength fits the island film radius, the electron resonantly populates the island film's state in the radial direction. Hence, the ion level decay occurs more efficiently, and we can see larger values of the ion level width. Therefore, the peaks in Fig. 8 are the results of the accidental match between island film radius and de Broglie wavelength in the radial direction. This also explains the periodic character of the H^- level width dependence ($\sim$20 a.u.).

V. RESONANT CHARGE TRANSFER FOR THE ASYMMETRICAL PROBLEM

For most of the examples in this section, the distance from the ion to the film symmetry axis is chosen as $X = +5$ a.u., which is much less than the island film radius 50 a.u.

A. Evolution of the electron density and ion state survival probability

Figure 9 represents the evolution of the electron density spatial distribution in the asymmetrical case. In said case, the electron density distribution evolution contains only three stages, because occupation of eigenstates along the ρ and φ coordinates begins in parallel. The first two stages are similar to the symmetrical case in that the electron distribution is continuous in the first stage and forms maxima along the z coordinate in the second stage. However, the third stage differs significantly in that the electron density exhibits maxima on the z, ρ, and φ coordinates.

Due to the broken symmetry, the correspondence of the electron density spatial distribution to the eigenstates is not as perfect as it is in the symmetrical case. However, the maxima near $\rho = 33$, 17, and 11 a.u. are clearly visible at the different times that correspond to $E = -1.21$, -1.19, and -1.32 eV, respectively. The energy spectrum of the autocorrelation function shows that compared to the symmetrical case, the peak $E = 1.36$ eV appears (Fig. 6).

Figure 10 demonstrates the survival probability of the H^- state as a function of interaction time for the symmetrical and asymmetrical cases. We see that in the asymmetrical case, the RCT process is also reversible, but it has a different oscillation period and character. There are periods when the electron is tunneling to the ion (at the moments $t \sim 1000$ and 2000 a.u.), but the amplitude of these back-tunneling peaks is small comparing to the symmetrical case. The reason for such alteration of RCT reversibility is that in the asymmetrical case, the "peripheral" state became populated earlier and intensively compared to the symmetrical case.

In Sec. III A, it was explained that electron reflection and backpropagation in the symmetrical case occur via "central" states (with maxima along the z-ρ coordinates only), and the electron from the peripheral states (with maxima along the z-ρ-φ coordinates) is not likely to transfer back to the ion. In the asymmetrical case, occupation of the "peripheral" states is greater compared to the symmetrical case. Due to the broken symmetry, the system is nondegenerate and the electron occupies "peripheral" states more intensively. In addition, contrary to the symmetrical case, during stages 1 and 2 the electron is forced to occupy the "central" states. However, due to electron wave-packet propagation, the asymmetrical system evolves to the electron density distribution close to the "central" state at times near 2650 a.u. (Fig. 9). As a result, we

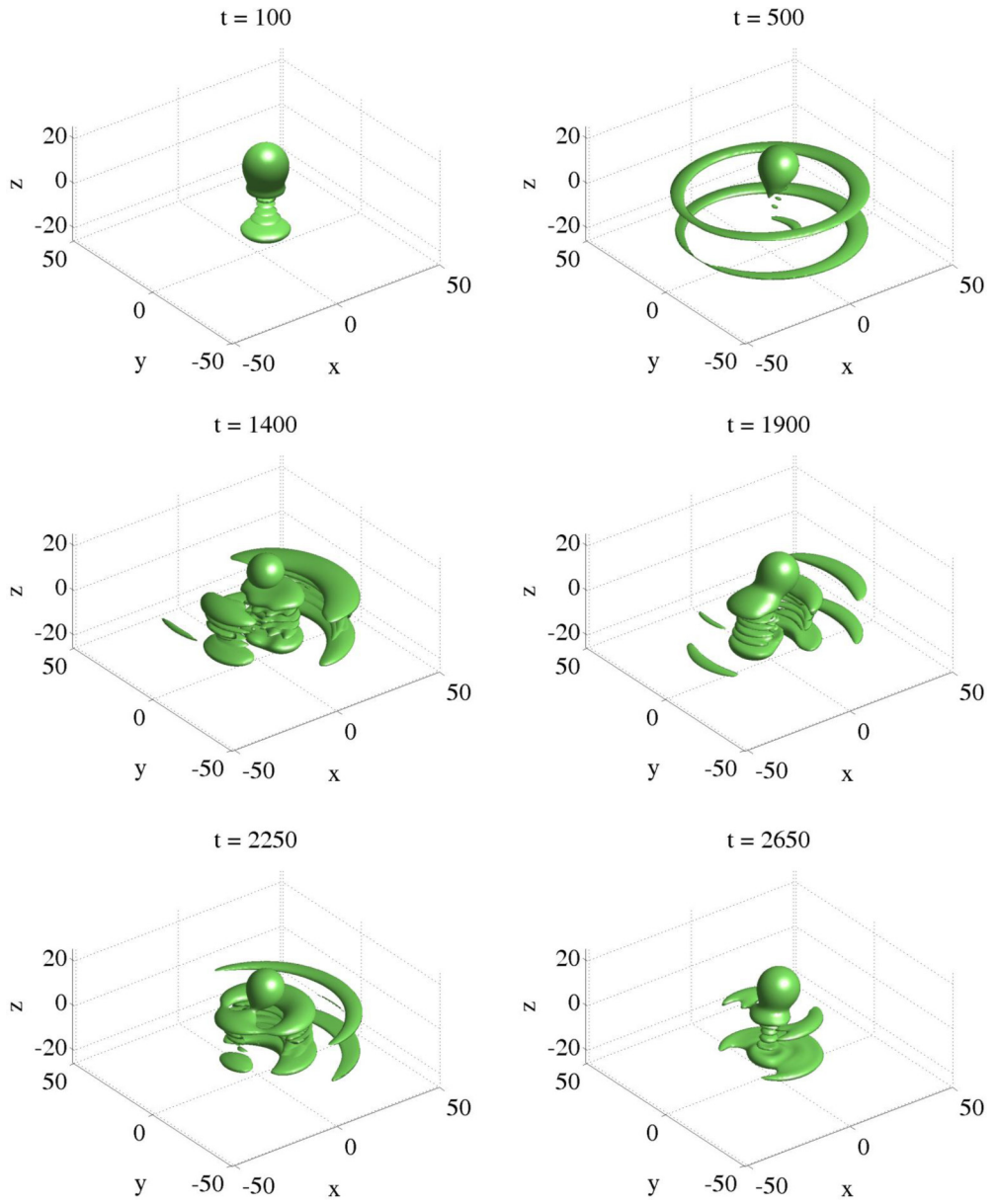

FIG. 9. (Color online) Isosurfaces of the electron density ($\rho = 0.0001$) at the subsequent moments of time for the asymmetrical case ($X = 5$). The ion coordinates are (5,0,12) a.u., and the island film borders are $z = 0$ a.u., $z = -15$ a.u., and $x^2 + y^2 = (50\,\text{a.u.})^2$. The values of the axes x, y, z and t moments are given in atomic units.

can see a great increase in the H^- ion survival state for the time ~3000 a.u.

Another characteristic feature of RCT in the asymmetrical case is that the electron current along the φ coordinate j_φ (φ current component) is much more than that in the symmetrical case, and its magnitude is comparable to the electron current along the z and ρ coordinates. Moreover, the j_φ exhibits anticorrelations with H^- ion survival probability. This indicates that high j_φ values are related to "peripheral" state occupation, and it proves the intuitive assumption that electron rotation around the center does not lead to backpropagation to the ion.

Finally, it should be stressed that a relatively small deviation from the symmetry axis ($X = 5 \ll R = 50$ a.u.) leads to a significant change in the electron evolution and RCT character.

B. Features of the quantum-size effect in the asymmetrical case

Figure 8 shows the H^- level width (RCT efficiency) as a function of the island film radius for the asymmetrical case. We see that this dependence exhibits the quantum-size effect as in the symmetrical case, but it is "softer." The possible explanation for this "softer" dependence is that due to the initial asymmetry of electron transition and localization, the resonance between the de Broglie wavelength and the island film radius became blurred.

Another interesting effect is the lateral dependence of the RCT efficiency (Fig. 11). We see that under a fixed nanosystem size and ion-surface distance, RCT efficiency can vary up to two times, depending on the ion's lateral position (the distance to the film's symmetry axis). This means that in the

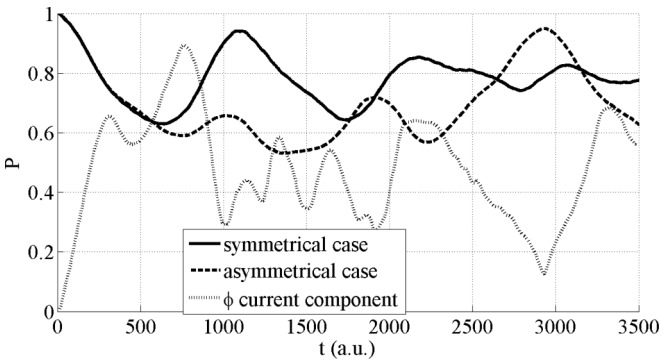

FIG. 10. Probability of the H^- state survival as a function of time. The solid line represents the result for the symmetrical case ($X = 5$), the dashed line represents the result for the asymmetrical case ($X = 5$), and the dotted line shows the φ component of the electron current in arbitrary units.

case of nanosystems, RCT efficiency depends not only on the ion-surface distance, but also on the ion's lateral position. Therefore, the projectile trajectory will have a great impact on the final charge state.

The explanation of the RCT lateral dependence is based on the spatial localization of "peripheral" states. Figure 11 also contains the averaged electron density distribution along the ρ coordinate for the "peripheral" states, which are participants in RCT. Despite the fact that this is a simple unweighted average, we can see an evident correlation with the maxima of RCT lateral dependence. On the qualitative level, RCT should be more efficient when the distance between the ion's location and the eigenstate's electron localization is minimal.

Note that the RCT lateral dependence was observed in Refs. [34,50], but here the lateral-dependent potential was used for modeling the solid body. In this study, we observe the RCT lateral dependence for the potential, which is constant along the surface.

C. Electron current evolution and quantum vortices

In the asymmetrical case, the averaged electron current distribution in the x-y plane has no axial symmetry. In this case, a very interesting phenomenon is observed, namely

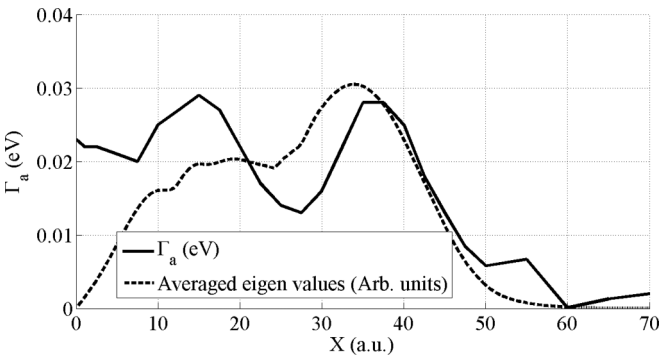

FIG. 11. H^- level width as a function of the distance between the atomic particle and the island film's symmetry axis (solid line). The dashed line shows the averaged ρ distribution of the 3D eigen wave functions (electron densities).

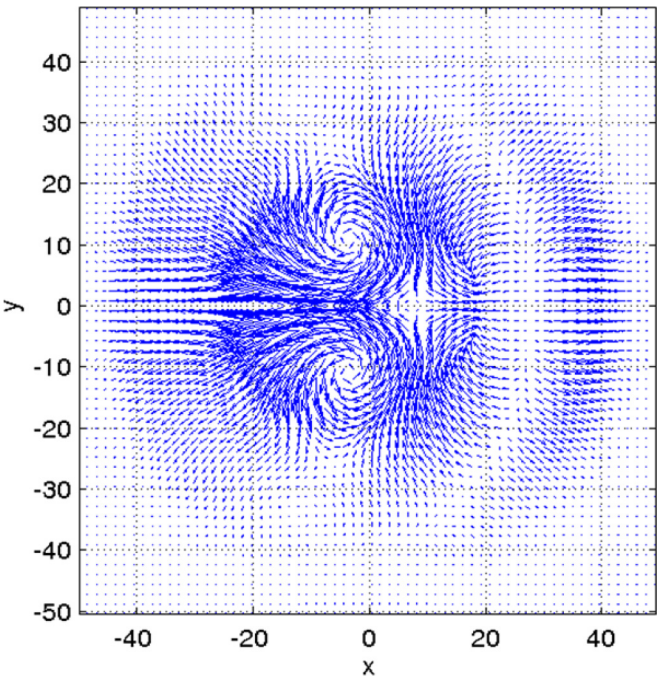

FIG. 12. (Color online) Illustration of quantum vortices arising in the asymmetrical case ($X = 5$). The figure shows the electron current averaged along the z coordinate at time 1500 a.u. The values of the x and y axes are given in atomic units.

quantum vortices (see Fig. 12). We can see that near points $x \sim -3.5$ a.u. and $y = +/-12$ a.u., the averaged current forms rotary fields, which are called quantum vortices. The origination of quantum vortices has been reported before [58], but the important difference is that in our case the quantum vortices appear in the static case (i.e., the Hamiltonian in the TDSE does not depend on time).

Figure 13 explains the formation of quantum vortices on a qualitative level. From the beginning of RCT, the electron predominantly occupies the right part of the film ($x > 0$), because the ion is located there. After the reflection from the right part of the island film, the radial boundary electron propagates parallel to the surface in the direction $x = -50$ a.u. After the reflection from the radial boundary, the electron begins the occupation of 3D eigenstates of the island film. The electron wave function can be treated as a superposition of several relevant eigenstates and a wave packet, moving parallel to the surface.

Up until $t = 450$ a.u., the system preserves symmetry with respect to the y axis, and the electron density distribution has branches/flows with radius ~33 a.u. This spatial localization is likely to be the "fingerprint" of the eigenstate with energy -1.21 eV (note that the same eigenstate dominates at $t = 500$ a.u. in the symmetrical case). At this period, the electron preferably propagates along the rings of the dominating eigenstate. Hence two branches of the electron density are forced to collide with each other in the region $y = 0$ ($t = 500$ a.u.). Because of this collision, the electron density flows are twisted to the center of the system, and we can see two quantum vortices ($t = 550$ a.u.). The electron density flows are twisted to the center because there are no eigenstates with

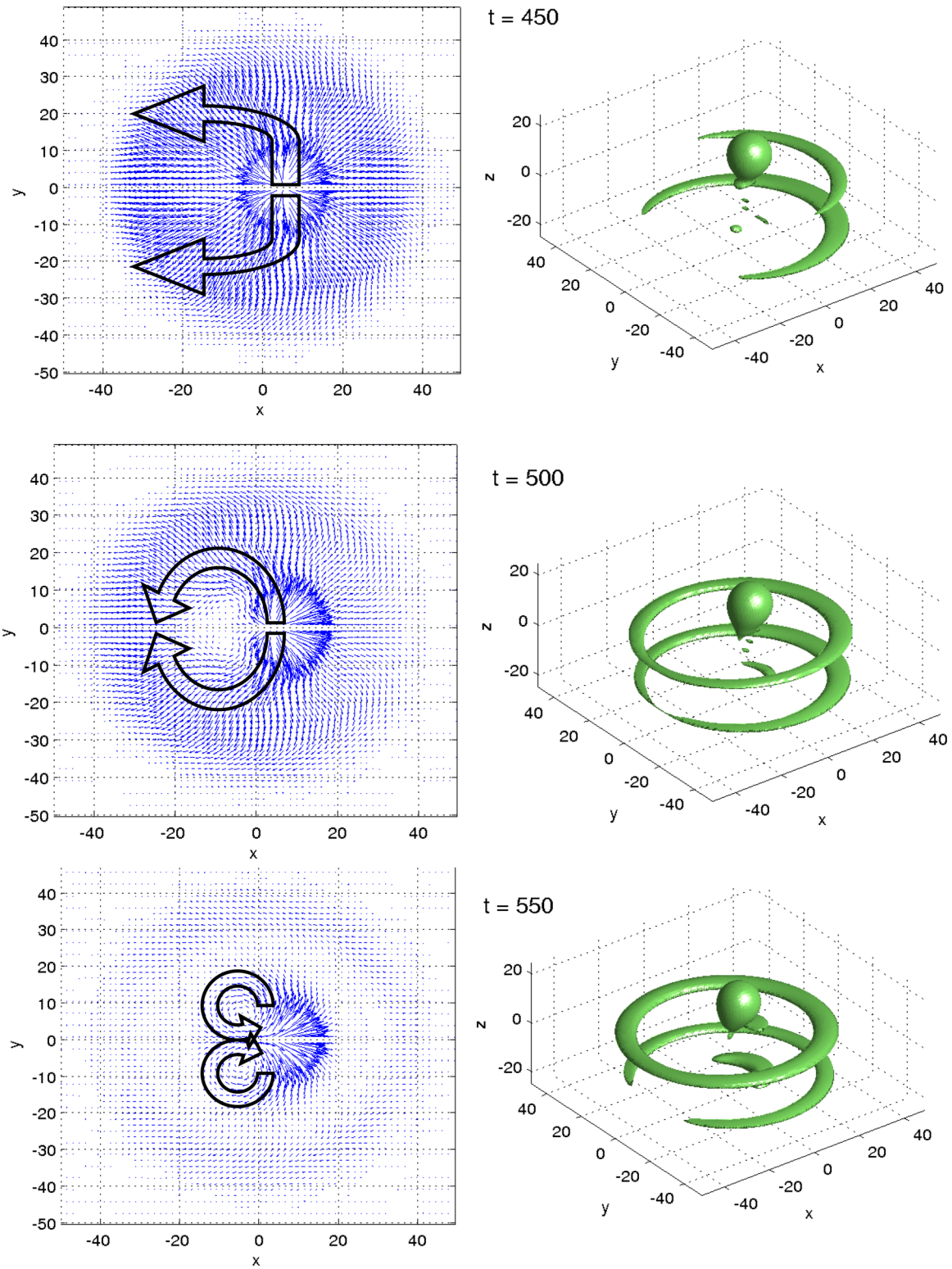

FIG. 13. (Color online) Formation of quantum vortices in the asymmetrical case ($X = 5$). The figure shows electron current averaged along the z coordinate at the subsequent moments of time. Curved arrows show the main direction of the electron's density movement. The ion coordinates are (5,0,12) a.u., and the island film borders are $z = 0$ a.u., $z = -15$ a.u., and $x^2 + y^2 = (50\,\text{a.u.})^2$. The values of the axes x, y, z and t moments are given in atomic units.

greater radius (see the sequence of the eigenstate occupation in Sec. III A).

After their formation, quantum vortices demonstrate dynamical stability for a relatively long period. For example, Fig. 14 illustrates the movement of quantum vortices. Two originated vortices are moving in the direction $x = +50$ a.u. The size and movement velocity of the vortices remain constant for the period from 600 to 800 a.u. The spatial

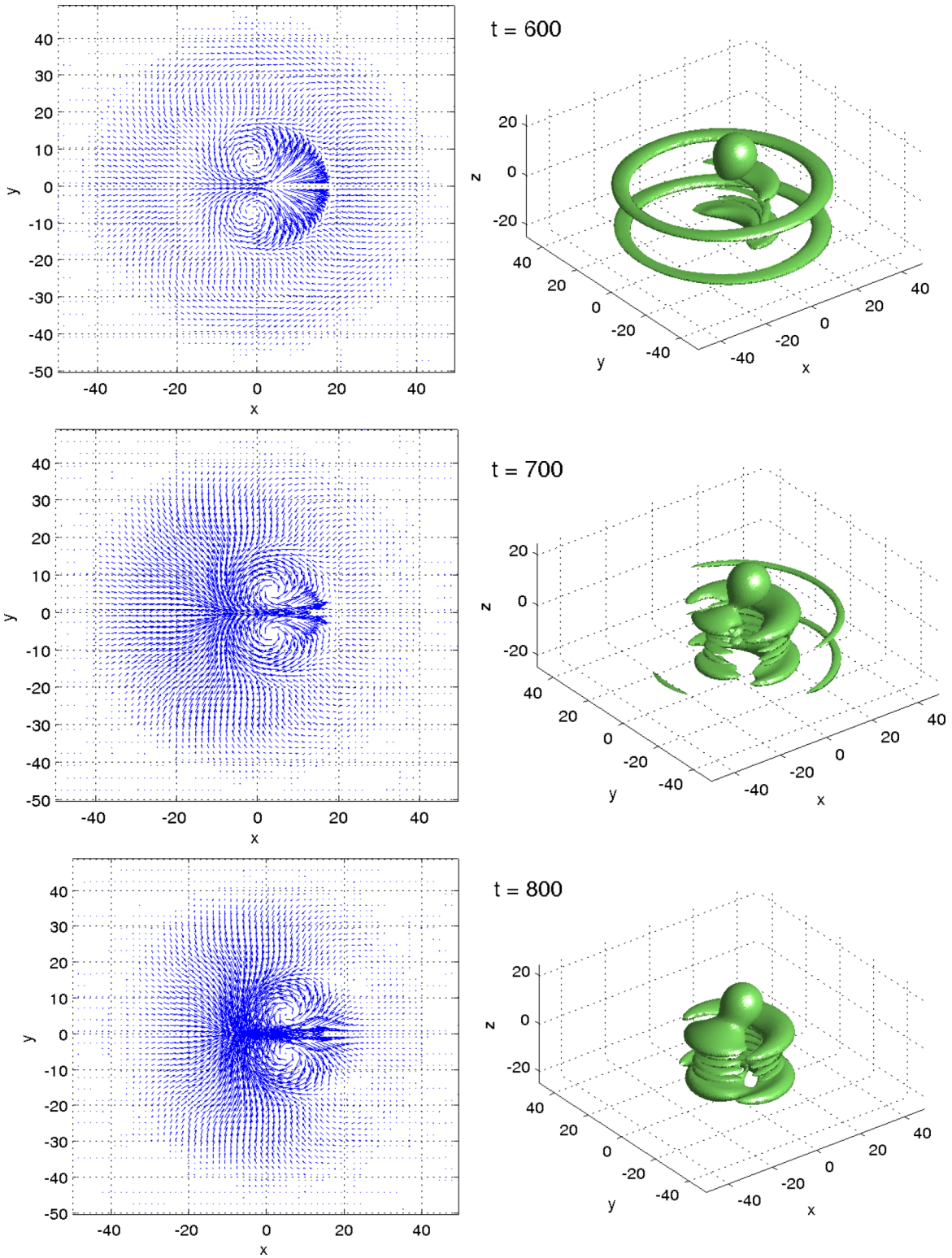

FIG. 14. (Color online) Evolution and movement of quantum vortices in the asymmetrical case ($X = 5$). The figure shows the electron current averaged along the z coordinate at the subsequent moments of time. The ion coordinates are (5,0,12) a.u., and the island film borders are $z = 0$ a.u., $z = -15$ a.u., and $x^2 + y^2 = (50\,\text{a.u.})^2$. The values of the axes x, y, z and t moments are given in atomic units.

electron localization during this period exhibits maxima for $\rho = 33$, 17, and 11 a.u. These are "fingerprints" of eigenstates with energy -1.21, -1.19, and -1.32 eV, respectively. For the period $t = 600-800$ a.u., we can observe the successive electron transition from eigenstate -1.21 eV to 1.19 eV and 1.32 eV, which is accompanied by the formation of quantum vortices. For the period $t = 800-1000$ a.u., the depicted quantum vortices hold their place and disappear after $t = 1000$ a.u., but the new vortices originate for the later times.

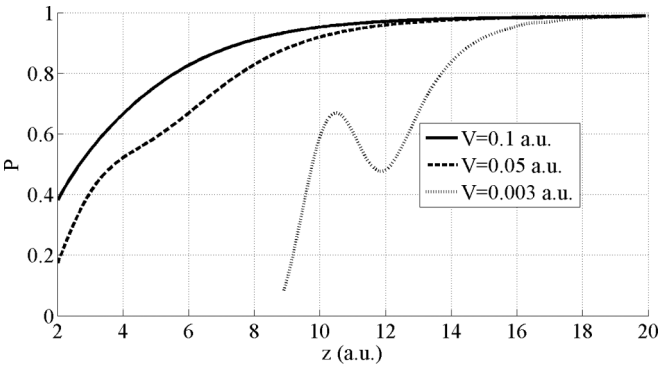

FIG. 15. Probability of the H^- state survival as a function of the distance to the surface for different projectiles velocities.

Note that the observation of quantum vortices in the static system is a very interesting result that could not be obtained by 2D calculations. Generally, it could be said that the times and localization of the quantum vortices are determined by the ion position and eigenstate localization inside the nanosystem. However, the regularities of the formation and evolution of quantum vortices require further investigation.

VI. RESONANT CHARGE TRANSFER FOR THE DYNAMIC PROBLEM

Finally, the developed TDSE solver was applied to the dynamic problem when a hydrogen ion approaches a thin island film with a constant velocity along the island film's symmetry axis. Figure 15 shows the ion survival probability as a function of the distance to the film surface for different projectile velocities. Similar calculations have been done for the 2D case in Ref. [45]. We see that for large velocities ($v >$ 0.1 a.u.), exponential decay takes place and the RCT process can be described by the rate equation $dP_{H^-}/dt = \Gamma(z)P_{H^-}$ (a comparison is given in [45]), while for small velocities ($v < 0.05$ a.u.), the ion occupation exhibits oscillations, i.e., reverse transitions of the electron from the nanosystem to the projectile take place. Such oscillations cannot be described by the rate equation under the adiabatic assumption. This illustrates the bottom limits of the applicability of the adiabatic approximation in the case of RCT with nanosystems. Of course, these limits depend on the nanosystem's size, especially its thickness along the z coordinate. For a film of 15 a.u. thickness, the limitation on the normal velocity is $v_\perp \geqslant 0.1$ a.u. This velocity value corresponds to the relatively small H ion energy 250 eV, but also to the significant 10 keV energy for Ar ions.

VII. CONCLUSIONS

This paper addresses a principal RCT features arising in nanosystems. To do this, we compared the RCT calculation results for the cylindrically symmetric problem (which have been well studied before) with the RCT calculation results for the asymmetrical problem (that was not extensively studied due to the numerical difficultness of the 3D calculations). The original high-performance numerical solver is used for the *ab initio* 3D RCT calculations.

The analysis of 3D eigen wave functions for thin metallic island film shows that there are two groups of eigenstates: (i) "central" states—when electron density is located near the symmetry axis and does not depend on the φ coordinate (these states are equal to the 2D eigenstates of the z-ρ coordinates); (ii) "peripheral" states—when electron density near the symmetry axis is close to zero and the eigen wave functions depend on the φ coordinate.

The electron density distribution inside the nanosystem is a superposition of densities of several relevant eigenstates and a moving part of the wave packet. The evolution of the electron density spatial distribution in the symmetrical case can be divided into four stages: in the first stage, the electron propagates without any restrictions, as in bulk metal, and in stages 2, 3, and 4 it successively occupies the nanosystem's eigenstates along the z, ρ, and φ coordinates, respectively. Of note, even under 2D initial conditions and potential (cylindrically symmetric), the system evolves to the 3D state with electron density maxima along all three coordinates. It should be noted that despite the occupation of the eigenstates, part of the electron wave function continues to move inside the nanosystem. Note that during the third stage, the electron density distribution does not depend on the φ coordinate, but the spatial localization of the electron density is close to the φ-dependent "peripheral" states rather than to the φ-independent "central" states. More surprising is that for the 2D calculations (z-ρ coordinates), the electron density maxima along the ρ coordinate also correspond to the 3D "peripheral" states. This happens because near the symmetry axis, the wave function is very volatile and the pseudo-3D states arise, which have localization close to the real 3D states but do not depend on the φ coordinate.

Another interesting feature of RCT in the symmetrical case is its "reversibility," i.e., in the first phase of interaction the electron decays from an atomic particle into the nanosystem, but in the second phase the reverse process begins, i.e., the electron moves back to the atomic particle. It should be noted that ion occupation has an oscillatory characteristic. The oscillation period is equal to the electron reflection time, and the oscillation amplitude depends on the RCT efficiency. The ion occupation exhibits anticorrelation with the occupation of "peripheral" states. This fact confirms that for the symmetrical problem ($X = 0$), RCT between the ion and the nanosystem occurs via "central" states. Note that due to the 3D effects, the oscillations in the 3D case fade more rapidly compared to the 2D calculations. In the asymmetrical case, the electron density distribution evolution contains only three stages, because occupation of eigenstates along the ρ and φ coordinates begins in parallel. In this case, the electron movement energy along the φ coordinate (which indicates the intensity of the 3D state occupation) is two orders of magnitude higher than that for the symmetrical case. The RCT process in the asymmetrical case is also reversible, but the oscillations are not as regular as in the symmetrical case. The ion occupation in the asymmetrical case exhibits anticorrelation with the electron movement energy along the φ coordinate.

The dependence of the RCT efficiency on the nanosystem size shows that it can vary up to four times. The maxima of RCT efficiency correspond to the resonant occupation of the island film's eigenstates in the radial direction. The

conditions for resonant occupation depend strongly on the island film radius. In the asymmetrical case, the RCT efficiency exhibits the quantum-size effect as well, but the dependence is weaker because of the blurring of the resonance conditions. In addition, it should be noted that under a fixed nanosystem size, the variation of the atomic particle's lateral position changes the RCT efficiency up to twofold. The maxima of the RCT efficiency's lateral dependence are related to the spatial localization of the eigenstates inside the nanosystem. This means that during ion-surface interaction, the nanosystem's size and the ion trajectory strongly influence the ion's final charge state.

In the asymmetrical case, the observation of quantum vortices in the static system is a very interesting result that cannot be obtained by 2D calculations. On a qualitative level, the formation of quantum vortices can be described by the collision of two electron density flows, which are bounded to the spatial localization of eigenstates inside the nanosystem.

The dynamical study of the RCT process between an ion and a nanosystem shows that for small projectile velocities (less than 0.1 a.u.), the ion occupation exhibits oscillations instead of exponential decay for large velocities. This means that in the case of nanosystems, the rate equation is applicable to the RCT problem only for relatively large projectile energies (greater than 250 eV for H and 10 keV for Ar).

ACKNOWLEDGMENTS

The authors gratefully acknowledge the financial support provided by the Russian Foundation for Basic Research (Grant No. 13-02-00879). The parallel computing facilities were provided by MV Lomonosov Moscow State University.

[1] R. Brako and D. M. Newns, Rep. Prog. Phys. **52**, 655 (1989).
[2] H. Shao, D. C. Langreth, and P. Nordlander, in *Low Energy Ion-Surface Interactions*, edited by J. W. Rabalais (Wiley, New York, 1994).
[3] T. Hecht, H. Winter, A. G. Borisov, J. P. Gauyacq, and A. K. Kazansky, Phys. Rev. Lett. **84**, 2517 (2000).
[4] J. P. Gauyacq, A. G. Borisov, and D. Teillet-Billy, in *Formation/Destruction of Negative Ions in Heavy Particle-Surface Collisions*, edited by V. A. Esaulov (Cambridge University Press, Cambridge, England, 1996).
[5] J. J. C. Geerlings and J. Los, Phys. Rep. **190**, 133 (1990).
[6] H. Chakraborty, T. Niederhausen, and U. Thumm, Phys. Rev. A **70**, 052903 (2004).
[7] R. J. Lad, Surf. Rev. Lett. **02**, 109 (1995).
[8] A. M. Azad, S. A. Akbar, S. G. Mhaisalkar, L. D. Birkefeld, and K. S. Goto, J. Electrochem. Soc. **139**, 3690 (1992).
[9] U. Kirner *et al.*, Sens. Actuators B **1**, 103 (1990).
[10] A. R. Canario, E. A. Sanchez, Yu. Bandurin, and V. A. Esaulov, Surf. Sci. Lett. **547**, L887 (2003).
[11] H. Chakraborty, T. Niederhausen, and U. Thumm, Phys. Rev. A **69**, 052901 (2004).
[12] T. Hetch, H. Winter, A. G. Borisov, J. P. Gauyacq, and A. K. Kazansky, Faraday Discuss. **117**, 27 (2000).
[13] R. Zimny, Surf. Sci. **233**, 333 (1990).
[14] J. P. Gauyacq, A. G. Borisov, and H. Winter, Comments At. Mol. Phys. **D2**, 22 (2000).
[15] M. Maazouz, A. G. Borisov, V. A. Esaulov, J. P Gauyacq, L. Guillemot, S. Lacombe, and D. Teillet-Billy, Phys. Rev. B **55**, 13869 (1997).
[16] L. Guillemot and V. A. Esaulov, Phys. Rev. Lett. **82**, 4552 (1999).
[17] J. Sjakste, A. G. Borisov, and J. P. Gauyacq, Nucl. Instrum. Methods Phys. Res. B **203**, 49 (2003).
[18] K. Niedfeldt, E. A. Carter, and P. Nordlander, J. Chem. Phys. **121**, 3751 (2004).
[19] A. R. Canario, A. G. Borisov, J. P. Gauyacq, and V. A. Esaulov, Phys. Rev. B **71**, 121401(R) (2005).
[20] B. Bahrim, B. Makarenko, and J. W. Rabalais, Surf. Sci. **594**, 62 (2005).
[21] B. Bahrim, S. Yu, B. Makarenko, and J. W. Rabalais, Surf. Sci. **603**, 703 (2009).
[22] R. A. Vidal, F. Bonetto, J. Ferron, M. A. Romero, E. A. Garsia, and E. C. Goldberg, Surf. Sci. **605**, 18 (2011).
[23] H. Zhou, L. Chen, D. Feng, Y. Guo, M. Ji, G. Wang, W. Zhou, Y. Li, L. Zhao, and X. Chen, Phys. Rev. A **85**, 014901 (2012).
[24] L. Chen, B. Ding, Y. Li, S. Qiu, F. Xiong, H. Zhou, Y. Guo, and X. Chen, Phys. Rev. A **88**, 044901 (2013).
[25] B. Bahrim and U. Thumm, Surf. Sci. **521**, 84 (2002).
[26] A. G. Borisov, D. Teillet-Billy, and J. P. Gauyacq, Phys. Rev. Lett. **68**, 2842 (1992).
[27] J. N. Bardsley, Case Stud. At. Phys. **4**, 299 (1974).
[28] P. J. Jennings, R. O. Jones, and M. Weinert, Phys. Rev. B **37**, 6113 (1988).
[29] E. V. Chulkov, V. M. Silkin, and P. M. Echenique, Surf. Sci. **437**, 330 (1999).
[30] A. G. Borisov, A. K. Kazansky, and J. P. Gauyacq, Surf. Sci. **430**, 165 (1999).
[31] P. M. Echenique and J. B. Pendry, J. Phys. C **11**, 2065 (1978).
[32] M. C. Desjonqueres and D. Spanjaard, *Concepts in Surface Science*, Springer Series in Surface Science Vol. 40 (Springer-Verlag, Berlin, 1993).
[33] B. Obreshkov and U. Thumm, Phys. Rev. A **74**, 012901 (2006).
[34] B. Obreshkov and U. Thumm, Phys. Rev. A **83**, 062902 (2011).
[35] B. Obreshkov and U. Thumm, Phys. Rev. A **87**, 022903 (2013).
[36] J. N. M. Van Wunnik, R. Brako, K. Makoshi, and D. M. Newns, Surf. Sci. **126**, 618 (1983).
[37] A. G. Borisov, D. Teillet-Billy, J. P. Gauyacq, H. Winter, and G. Dierkes, Phys. Rev. B **54**, 17166 (1996).
[38] I. K. Gainullin and I. F. Urazgildin, Izv. RAN, Ser. Fiz. **70**, 897 (2006) [Bull. Russian Acad. Sci., Phys. **70**, 1024 (2006)].
[39] I. K. Gainullin, E. Yu. Usman, and I. F. Urazgildin, Nucl. Inst. Meth. B **232**, 22 (2005).
[40] I. K. Gainullin, E. Yu. Usman, Y. W. Song, and I. F. Urazgil'din, Vacuum **72**, 263 (2004).
[41] U. Thumm, P. Kurpick, and U. Wille, Phys. Rev. B **61**, 3067 (2000).
[42] E. Yu. Usman, I. F. Urazgil'din, A. G. Borisov, and J. P. Gauyacq, Phys. Rev. B **64**, 205405 (2001).
[43] E. R. Amanbaev, I. K. Gainullin, E. K. Zykova, and I. F. Urazgildin, Thin Solid Films **519**, 4737 (2011).

[44] I. K. Gainullin, K. K. Satarin, E. Yu. Usman, and I. F. Urazgildin, J. Surf. Invest. **1**, 39 (2005) (in Russian).
[45] I. K. Gainullin and I. F. Urazgildin, Phys. Rev. B **74**, 205403 (2006).
[46] A. A. Magunov, D. K. Shestakov, I. K. Gainullin, and I. F. Urazgildin, J. Surf. Invest. **9**, 93 (2008) [J. Surf. Invest.: X-Ray, Synch. Neutron Tech. **2**, 764 (2008)].
[47] D. K. Shestakov, T. Yu. Polivnikova, I. K. Gainullin, and I. F. Urazgildin, Nucl. Instrum. Methods, Phys. Res. B **267**, 2596 (2009).
[48] A. R. Canario and V. A. Esaulov, J. Chem. Phys. **124**, 224710 (2006).
[49] A. R. Canario, T. Kravchuk, and V. A. Esaulov, New J. Phys. **8**, 227 (2006).
[50] M. Taylor and P. Nordlander, Phys. Rev. B **64**, 115422 (2001).
[51] U. Thumm, https://jrm.phys.ksu.edu/Research/Meetings/DOE-AMOP/ut.pdf.
[52] I. K. Gainullin and M. A. Sonkin, Comput. Phys. Commun. **188**, 68 (2015).
[53] E. Y. Zykova, A. A. Khaidarov, I. P. Ivanenko, and I. K. Gainullin, J. Surf. Invest. **11**, 7 (2012) [J. Surf. Invest.: X-Ray, Synch. Neutron Tech. **6**, 877 (2012)].
[54] V. A. Ermoshin and A. K. Kazansky, Phys. Lett. A **218**, 99 (1996).
[55] J. S. Cohen and G. Fiorentini, Phys. Rev. A **33**, 1590 (1986).
[56] C. Leforestier, R. H. Bisseling, C. Cerjan, M. D. Feit, R. Friesner, A. Guldberg, A. Hammerich, G. Jolicard, W. Karrlein, H. D. Meyer, N. Lipkin, O. Roncero, and R. Kosloff, J. Comput. Phys. **94**, 59 (1991).
[57] E. R. Amanbaev, E. Yu. Zykova, A. L. Klavsjuk, T. N. Polivnikova, A. A. Khaidarov, and I. K. Gainullin, J. Surf. Invest. **7**, 70 (2011) (in Russian).
[58] J. H. Macek, J. B. Sternberg, S. Y. Ovchinnikov, T. G. Lee, and D. R. Schultz, Phys. Rev. Lett. **102**, 143201 (2009).